CEAS Aeronaut J (2014) 5:403–417
DOI 10.1007/s13272-014-0115-2

ORIGINAL ARTICLE

SFB 880: aeroacoustic research for low noise take-off and landing

J. Delfs · B. Faßmann · N. Lippitz · M. Lummer · M. Mößner · L. Müller · K. Rurkowska · S. Uphoff

Received: 17 December 2013 / Revised: 14 May 2014 / Accepted: 26 May 2014 / Published online: 19 June 2014

Abstract This paper gives an overview about prediction capabilities and the development of noise reduction technologies appropriate to reduce high lift noise and propeller noise radiation for future low noise transport aircraft with short take-off and landing capabilities. The work is embedded in the collaborative research centre SFB 880 in Braunschweig, Germany. Results are presented from all the acoustics related projects of SFB 880 which cover the aeroacoustic simulation of the effect of flow permeable materials, the characterization, development, manufacturing and operation of (porous) materials especially tailored to aeroacoustics, new propeller arrangements for minimum exterior noise due to acoustic shielding as well as the prediction of vibration excitation of aircraft structures, reduced by porous materials.

Keywords Aeroacoustics · Porous materials · Trailing edge noise · Acoustic shielding · Channel wing

This paper is based on a presentation at the German Aerospace Congress, September 10–12, 2013, Stuttgart, Germany.

J. Delfs (✉) · B. Faßmann · M. Lummer
Institute of Aerodynamics and Flow Technology (IAS), DLR Braunschweig, Braunschweig, Germany
e-mail: jan.delfs@dlr.de

N. Lippitz
Institut für Werkstoffe Technische Universität Braunschweig (IW), Braunschweig, Germany

M. Mößner · L. Müller
Institute of Fluid Mechanics, Technische Universität Braunschweig (ISM), Braunschweig, Germany

K. Rurkowska
Institut für Konstruktionstechnik, Technische Universität Braunschweig (IK), Braunschweig, Germany

S. Uphoff
Institut für Rechnergestützte Modellierung im Bauingenieurwesen (IrMB) Technische Universität, Braunschweig, Germany

1 Introduction

Within the TU Braunschweig-led "Coordinated Research Centre SFB 880" a new transport aircraft segment is investigated for use on airports with shorter runway length and for operations much closer to the home of its passengers than today possible. This new class of aircraft is subject to considerably more stringent limits on noise emission than today's aircraft. In SFB 880, a turboprop driven high wing aircraft equipped with an active circulation controlled high lift system is considered the most appropriate concept to simultaneously meet the—seemingly contradicting—requirements of short runway and low noise. Research area A of SFB 880 designated "Fundamentals of Aeroacoustics" develops an integrated aeroacoustic and aerodynamic design methodology to include advanced source noise mitigation measures such as porous surfaces as well as engine integration concepts which reduce radiation to the ground.

The acoustic challenges for the SFB 880 aircraft are twofold:

1. Airframe noise, typically generated by the landing gear and the high lift devices, is dominating at approach condition and needs to be reduced considerably. Generally the landing gear is an important contributor to airframe noise. However, technologically feasible low noise solutions have already been developed in the past and wait for an implementation such that these are

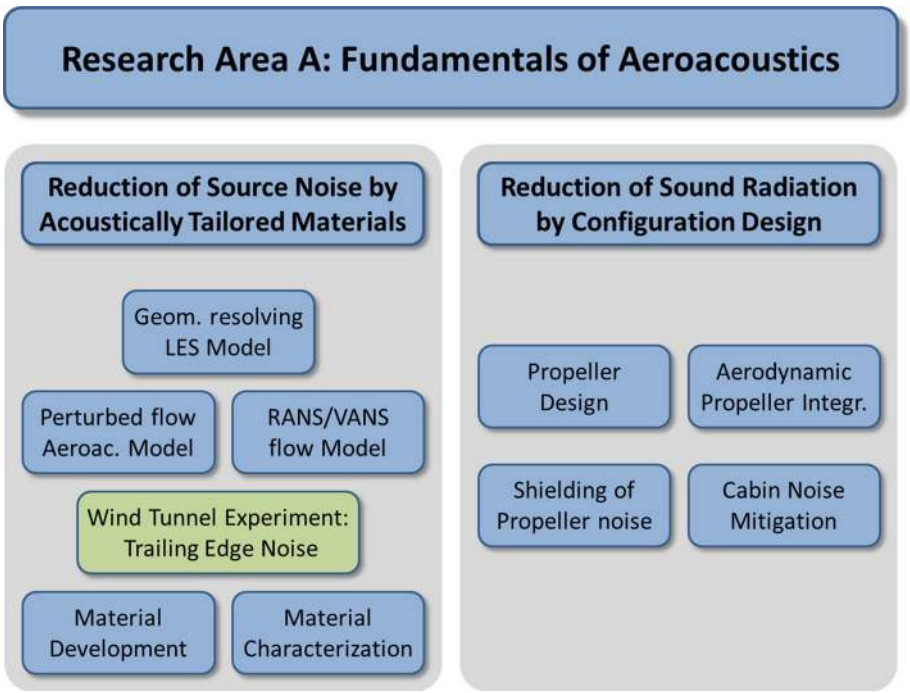

Fig. 1 Structure of aeroacoustic research for low noise SFB aircraft for the first 4 years

of minor interest for current research on airframe noise reduction. The understanding and reduction of high lift noise caused by the turbulent flow past the high lift device components remains a major challenge.

2. Propeller noise is responsible for the aircraft noise at take-off. Its radiation to the ground needs to be reduced considerably.

Both challenges are aggravated by the fact that the aerodynamic performance must not be compromised, whatever measure is taken to reduce the noise.

Research area A therefore deals with exploring ways to reduce the noise of aircraft of the mentioned kind. As the two columns in the overview chart of Fig. 1 indicate, two key technologies for the reduction of community noise were identified. First, materials have to be specified, predicted and developed, which reduce the turbulence related high lift noise generation at the source. Simultaneously, acoustic shielding effects of the aircraft configuration on the groundward radiation of unavoidable propeller noise need to be exploited by favorable propulsion/airframe integration. Since the overall aircraft design is subject to the implicit interdependencies of technologies also the important influences are explored, which the reduction technologies for exterior noise have on the aircraft's cabin noise. The work in area A is structured into six research projects.

In what follows, Sect. 2 discusses the research challenges associated with source noise reduction by means of aero-acoustically tailored materials. Results of the various contributing research branches are presented. Section 3 is devoted to a configuration study on a propeller/wing integration, especially focused on maximum noise shielding. The conclusions are discussed in Sect. 4.

2 Airframe noise reduction by acoustically tailored materials

High lift devices are operating in the free air with a direct line of sight to the observer at the ground. This circumstance rules out any "classical" means of noise reduction by encapsulating the source or using liners to absorb the sound (secondary noise control). Work has to concentrate rather on the reduction of the sound generated, i.e. manipulation of the source of sound (primary noise control). High lift noise is a result of the presence of turbulence adjacent to leading-, trailing-, side edges and slots and is therefore highly difficult to predict and to reduce. First Computational Aeroacoustics Methods (CAA) have successfully been developed to enable design studies for low noise slat settings [4]. However, the success is usually limited due to reverse effects on the aerodynamic performance.

The by far most successful means of reducing high lift noise is believed to lie in the use of permeable edge extensions or permeable edge materials. Broadband noise reduction on the order of 10–13 dB was achieved with brush trailing edge extensions on airfoils [2]. Also slotted edges or flow permeable materials show considerable noise reduction potential [1]. However, the reduction mechanism of these measures is not understood and therefore it is

unclear, how to use these means appropriately. Therefore research was initiated, covering the various aspects of materials, capable of reducing the sound generation of airframe noise, which is entirely different from the action of classical sound absorbers. The key aspect in this field are (1) the aeroacoustic simulation of the effect of permeable materials below turbulent boundary layer flow, and (2) the corresponding characterization, development, manufacturing and operation of (porous) materials especially tailored to aeroacoustics.

2.1 Prediction of flow noise reduction by permeable materials

Two different computation approaches are being developed in area A to predict the reduction of the sound radiation from high lift devices. The first approach pursued by IAS and designed for the noise prediction in high Reynolds number flows, is based on simulating with the high resolution DLR CAA Code PIANO [4] the inviscid dynamics of unsteady vortical and acoustic perturbations to a precomputed, time-averaged [Reynolds-averaged Navier–Stokes (RANS)] flow field. As a preliminary step this hybrid approach requires a RANS flow field which was generated by ISM with DLR CFD solver TAU [9] as an input for the perturbation equations. In either step (CFD and CAA) the flow permeable (fine scale) material is not resolved but described in a volume-averaged sense which requires the development and implementation of a respective model.

The second approach pursued by IrMB relies on the numerical solution of the Boltzmann equation by means of the Lattice Boltzmann Method. Like in a Large Eddy Simulation (LES), the turbulent flow is resolved down to a small scale beyond which a subscale model is employed; the individual pores of the permeable material below the turbulent boundary layer are individually resolved. The description of the material therefore does not require any separate modeling. This second computation approach is used as a reference for at least partial validation of the first approach, which involves modeling simplifications to the flow and the porosity.

2.1.1 Study on source noise reduction by slits

IAS carried out a first study to identify the relevant mechanism responsible for the source noise reduction by a permeable material. These fundamental investigations were done on the trailing edge noise problem of a simple airfoil at zero angle of attack. The working hypothesis was that three colluding fundamental mechanisms may be responsible for the sound reduction of trailing edge sound linked to porous material: (a) The change of turbulence production due to the porosity, (b) acoustic absorption and (c) the change of sound generating process at the trailing edge. The following section will present the results of a systematic study of the three mechanisms in relation to former experimental findings.

In order to avoid any modeling approximation of a porous material the simple flow permeable arrangement of narrow lengthwise slits [1] was investigated, which was spatially resolved in the simulations for a Ma = 0.12 free stream flow speed. Previous measurements showed a 6 dB broadband trailing edge noise reduction for such slits [2]. The slits are fully permeating the trailing edge of a NACA0012 airfoil from lower side to upper side. They have a width of 0.1 mm and are simply applied to the rear part of the airfoil: 11.25 % of the chord length $c = 0.4$ m. The slits are evenly distributed in spanwise direction and are separated by non-slotted sections of 0.4 mm width. Thus they have a periodic distance of 0.5 mm. The acoustic results are always compared to a reference case of a completely solid trailing edge.

The potential mechanisms are analysed systematically by means of Computational Fluid Dynamics (CFD) and Computational Aero-Acoustics (CAA). Periodic boundary conditions were used to represent an infinite span with slits in order to save computation time.

Only one slit and the half of the two adjacent solid struts are comprised within the computational domain for CFD and CAA, see Fig. 2. The CFD was carried out using the $k - \omega$ turbulence model.

The CFD results showed no significant impact of the narrow slits on the mean flow velocity profiles. A "driven cavity"-like recirculation bubble inside the slit is observed with flow speeds ranging from a maximum of 1.6 ‰ of the free stream speed in the upstream part of the slit to a maximum of less than 2 % near the trailing edge. Any deviations from the no-slip mean profiles of the solid trailing edge are correspondingly small. As a consequence the boundary layer turbulence quantities are hardly

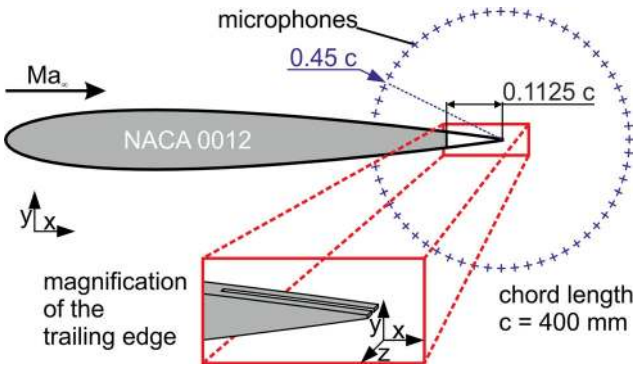

Fig. 2 Computation setup for trailing edge noise reduction simulation

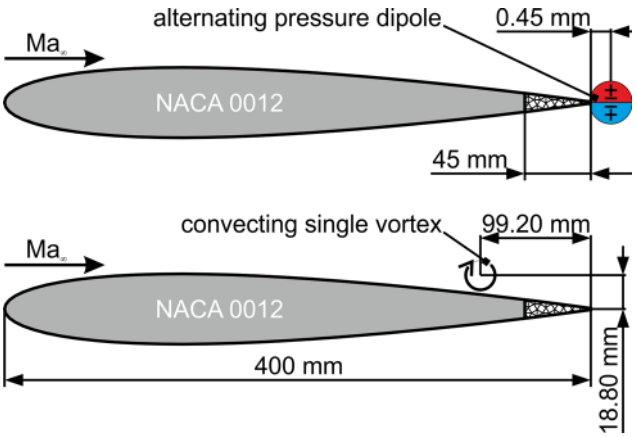

Fig. 3 Numerical implementation of the edge dipole (*top*) and the advecting single vortex (*bottom*), see also [3]

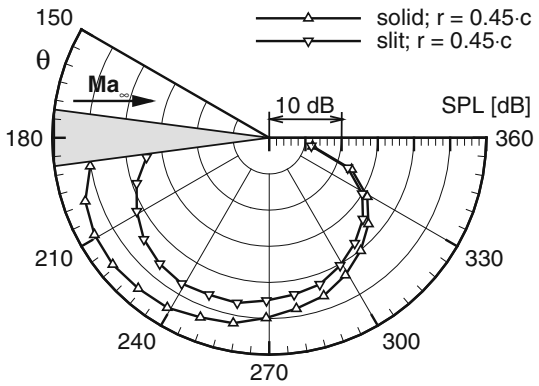

Fig. 4 Directivity of the trailing edge sound generated by an edge dipole (only lower part shown because of symmetry, see also [3])

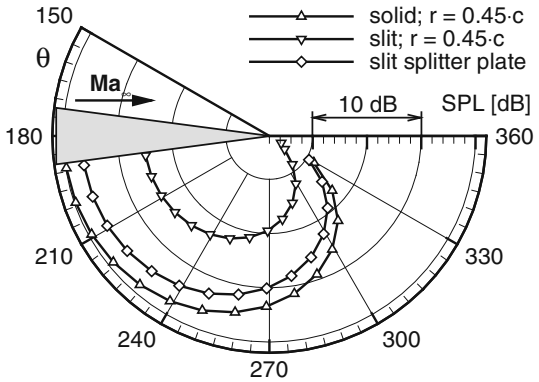

Fig. 5 Directivity of the trailing edge sound generated by an advecting single vortex, see also [3]

influenced by the slits. Since the mean flow shear and the turbulence intensity as relevant source parameters for trailing edge noise turned out to be practically invariant under the introduction of the slits considered, it was concluded that the mechanism (a) cannot be responsible for the experimentally observed noise reduction.

In order to investigate hypotheses (b) and (c) two distinctly different aeroacoustic simulations were carried out: On the one hand, a non-vorticity related time periodic acoustic source was generated with a dipole directivity centered at the trailing edge point and with a dipole axis normal to the edge and the flow. This situation was chosen to investigate any possible absorption effect of the slits on an existing generically acoustic field, characteristic for trailing edge noise, i.e. being in anti-phase on top and bottom side of the airfoil. On the other hand, a single advecting vortex was initialised in the boundary layer well upstream of the slotted (porous) trailing edge section. According to the presence of the flow this vortex perturbation moves past the trailing edge, where its induced velocity perturbation around the edge generates a pressure field, which in turn excites pressure pulses radiated away as sound. This situation was chosen to represent the aeroacoustic edge sound generation process (conversion of vortical into acoustic perturbations) with and without slits. Both simulation situations are sketched in Fig. 3.

The simulations with the edge dipole predict the sound reduction to be clearly dependent on the observer position, see Fig. 4, showing the directivity at an edge distance of 45 % of the chord length c. The strongest reduction effect of roughly 6 dB is perceived in the upstream direction, while at 90° below the trailing edge, the benefit is only 2.3 dB. The anti-phase pressure signals of upper and lower side partly annihilate through the slit, which is responsible for the reduction of the radiated sound. The fact that this signal cancellation takes place in the near field of the source leads to a reduction of the overall sound power radiated to the far field quite similar to the overall sound power of two anti-phase monopoles at small distances. The pressure cancellation applies for the vertical and the upstream direction, while in the downstream direction, annihilation occurs anyway.

The simulations with the single vortex (Fig. 5) show a weaker dependency of the sound reduction on the observation angle. The sound reduction due to the slits amounts to 6 dB for most of the acoustic field in remarkable correspondence to the experimental findings in [2]. Sound reduction not only occurs in the upstream direction but in the vertical direction, as well. Even in the downstream direction, partly a reduction of 5 dB is perceivable.

Application of a splitter plate into the slit which is preventing any vertical perfusion flow through the slit, almost leads to a total loss of the acoustic benefit of the porosity. Just as the findings for the acoustic dipole source indicated, the ventilation of the source (near field) pressure through the slits is instrumental for the reduction of the sound radiation. This shows that the porosity cannot be

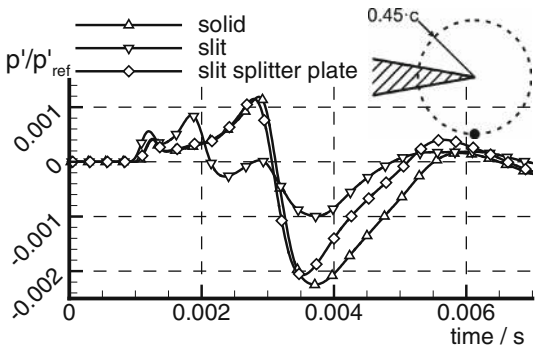

Fig. 6 Time signal of the fluctuating pressure at a microphone position 90° below the trailing edge during the passage of a single vortex, $p'_{\mathrm{ref}} = \rho_\infty U_\infty v'_{\mathrm{max}}$ where v'_{max} is maximum speed perturbation induced by initial vortex

modelled in terms of locally reacting classical impedance boundary conditions but require a volume-averaged CAA approach.

In Fig. 6, a second effect of the slits is illustrated: A fully permeable slit evokes two sound events: One at the upstream onset of the porous region and another one at the actual trailing edge of the airfoil. Since sound is generated at each (leading and trailing) edge perpendicular to the mean flow the simulation indicates that materials with a flow aligned permeability like the considered slits are most effective due to their minimum accumulated length of all such edges when compared to any other material with the same porosity.

2.1.2 *Simulation of mean flow in the presence of porous materials*

The CAA perturbation simulations for the sound prediction rely on the availability of a time-averaged mean flow field along with statistical turbulence information provided by the turbulence model. Moreover, any change in the mean flow according to the presence of permeable material will potentially have an effect on the aeroacoustics. Therefore the objective of the work of ISM is the provision of tools to simulate turbulent flow over airplane configurations with porous surface inserts. The Mach number of the configurations is high enough that compressibility effects have to be taken into account. The capability of simulating flow over porous media is needed in the context of the SFB 880 because the important target of noise reduction relies substantially on the presence of porous surfaces. The collaboration with other SFB projects allows thorough validation of the developed tools. These projects supply data by investigating the porous surface flows with experiments and DNS computations.

Basic principles used to simulate flow over porous media. The characteristic length of the porous structures suited for noise reduction is very small compared to the characteristic lengths of the investigated airplanes. Also, the Reynolds numbers of the airplanes are in the range where the flow is fully turbulent. These two predefinitions lead to the difficulty that both the turbulent structures and the flow through the porous structure cannot be resolved. These problems are solved by employing averaging methods. Volume averaging inside the porous medium leads to additional terms in the Navier–Stokes equations which take account for the drag that results from the flow through the porous structure (e.g. see [5]). Time averaging causes the well-known Reynolds stress terms of the Reynolds-averaged Navier–Stokes equations (e.g. see [6]).

The Reynolds stresses are obtained by using a Reynolds stress turbulence model (homogeneous Jakirlic and Hanjalic JHh Version 2 [7]). It consists of seven transport equations which are extended by additional terms originating from averaging over the porous structure.

An additional difficulty is the interface area between the porous and the nonporous region. The flow across this interface area is basically described by an isentropic flow change. The diffusive fluxes caused by spatial gradients of the flow variables are corrected using a stress jump condition over the interface [8].

Current progress and validation. The theoretical considerations as described above are implemented in the DLR flow solver TAU [9]. This is a well established solver based on the finite volume method. First test cases are now running and they show good behaviour in spatial and iterative convergence.

The validation case shown in here is a channel flow where the lower half of the channel is filled with a generic porous structure of cubes (see Fig. 7). The side walls are

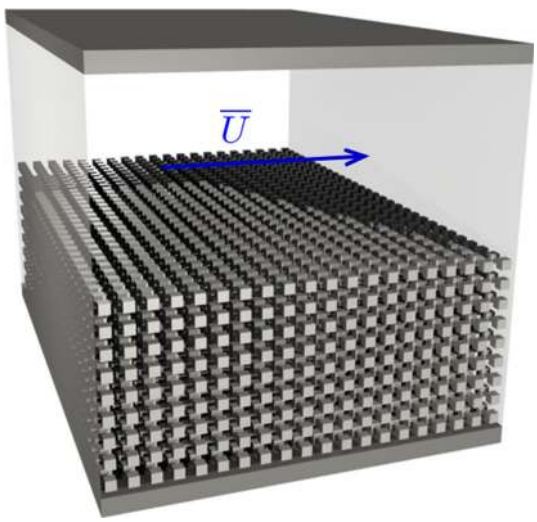

Fig. 7 Validation case of channel where lower half is filled with "hovering" cubes, representing porous material

defined as symmetric boundary conditions to give the channel a 2-dimensional character. The Reynolds number $Re = \bar{U}h/\nu$ based on the nonporous channel height h and the averaged velocity $\bar{U}$ in the nonporous section is $Re = 5{,}500$. The Darcy number $Da = \kappa/h^2$ of the porous structure is based on the same channel height h and the permeability κ and has the value of $\mathrm{Da} = 3.4 \times 10^{-4}$. The channel setup is taken from [10] as it provides DNS data for this case.

Some results are shown in Fig. 8. The velocity profile reduces to quite small numbers inside the porous region due the high drag of the cubes. Also the Reynolds stresses diminish rapidly inside the porous region; however, an over prediction of the damping can be seen for the RANS computation. The reason for this local suppression of turbulence is not clear yet. There are several modelling parameters which still have to be adjusted and could improve the behaviour. Also more validation cases are available and will be tested to obtain the sensitivities with respect to the different modelling terms.

The modeling of turbulent flow through porous media by using a volume and time averaging approach give already good results for the turbulent channel flow with a partially porous flow domain. Especially in the nonporous region the results agree very well with DNS data (see also [11]).

In the future flow over a porous flat plate and flow over a wing with a porous trailing edge will be measured in a wind tunnel and these serve as reference cases for more validations. Also, the flat plate will be computed with DNS. The DNS will yield information about the flow inside the porous region of the flat plate.

2.1.3 *Lattice Boltzmann LES simulation of flow past porous materials*

IrMB conducts highly resolved simulations of turbulent boundary layers, flow in resolved porous media and acoustics. These simulations are based on the Lattice Boltzmann method (LBM), which, due to the underlying Cartesian, block structured grids is particularly apt for the simulation of pore-resolved flows. This project supplies flow parameters for other subprojects, e.g. boundary layer parameterizations for the RANS/VANS (closure of Reynolds stress models in 2.1.2) as well as permeability and tortuosity for the material characterization in 2.1.4.

Determination of microscopic parameters. First, the permeability of the samples considered in this work is determined numerically using the LB method, as described in [12]. The results are being compared to measurement data obtained in the project on vibroacoustics (see Sect. 2.2.2). CT scans have been derived in the project of the IW (Sect. 2.1.4), from which the numerical setup is constructed. For the sintered felts the geometry is reflected in both directions normal to the mean flow direction in order to construct a continuous geometry that can be extended periodically. In flow direction a pressure gradient is applied using pressure boundary conditions. From the converged flow field the Darcy-velocity can be computed, which in turn allows to compute the flow resistance. Flow resistivity values were measured by the Physikalisch Technische Bundesanstalt—PTB in Braunschweig using the alternating airflow method according to DIN EN 29053, Method B. The results are given in Table 1. Throughout the paper following notations are used for the various materials:

MPP: microperforated sheet metal
MPP1: MPP with large long holes
MPP2: MPP with narrow long holes
MPP3: MPP with large circular holes
MPP4: MPP with small circular holes
SFF100 150: sintered fibre felts 100, 150
M450: metallic foam

In a similar way additional characteristics of porous media, such as the tortuosity or the surface roughness of the porous media (see Fig. 9), have been determined.

Flow around a flat plate. The flat plate turbulent boundary layer is a standard test case in CFD, e.g. [14], but

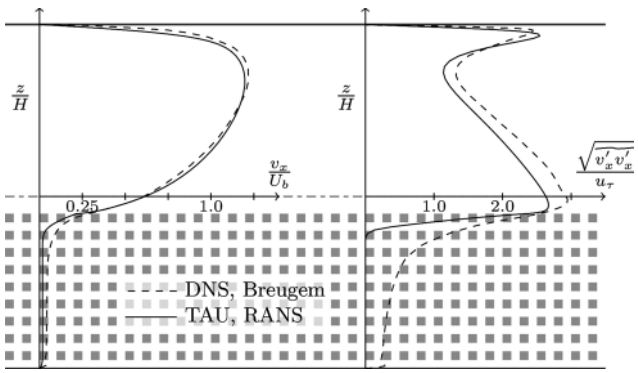

Fig. 8 Comparison of results of partially porous channel flow. DNS against the newly implemented TAU-implementation

Table 1 Flow resistance divided by the probe thickness (resistivity σ) for the different materials investigated in (Sect. 2.1.4): comparison of simulation results (Sim) with experimental values (Exp)

Sample	Exp (Pa s/m^2)	Sim (Pa s/m^2)	Error (%)
MPP1	9.42×10^4	1.47×10^5	56
MPP2	3.66×10^5	3.70×10^5	1
MPP3	2.35×10^5	2.20×10^5	−7
MPP4	7.67×10^5	7.02×10^5	−13
SFF100	5.70×10^4	3.50×10^4	−63
SFF150	1.89×10^4	1.99×10^4	5
M450	1.10×10^4	9.59×10^4	−15

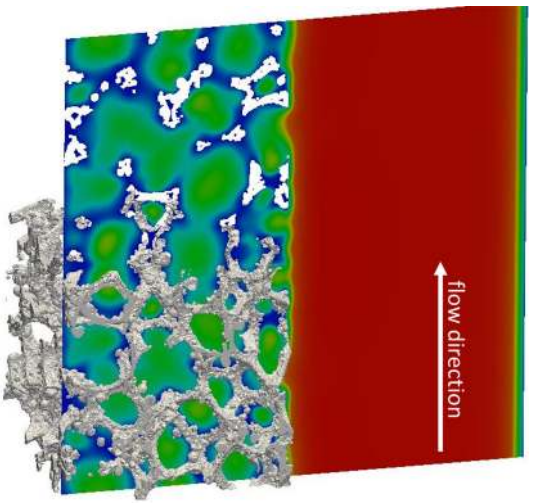

Fig. 9 Visualization of the magnitude of the flow speed for parallel flow past the metal foam M450

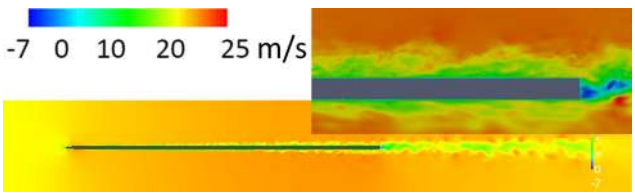

Fig. 10 Visualization of the instantaneous speed of turbulent flow around the flat plate

Table 2 Simulation parameters flat plate

Parameter	Value
Reynolds number based on plate length	1.13×10^6
Inflow velocity	17 m/s
$\triangle x_{\text{fine}}$	0.000234283 m
$\triangle t_{\text{fine}}$	3.98×10^{-7} s
Domain extension	$2.25 \times 0.6 \times 0.0825$ m
Length of the plate	1 m
Number of grid nodes (degrees of freedom)	2.38×10^8
Simulated real time	0.48 s

has rarely been studied with LBM. With DNS and LES techniques the transition from laminar to turbulent flow can be examined. In contrast to fully developed turbulent channel flow, the boundary layer has a finite thickness, outside of which the flow remains undisturbed (see Fig. 10). The simulation was carried out using with the MPI-parallel code VirtualFluids [13]. The relevant parameters are given in Table 2. The D3Q19 MRT model

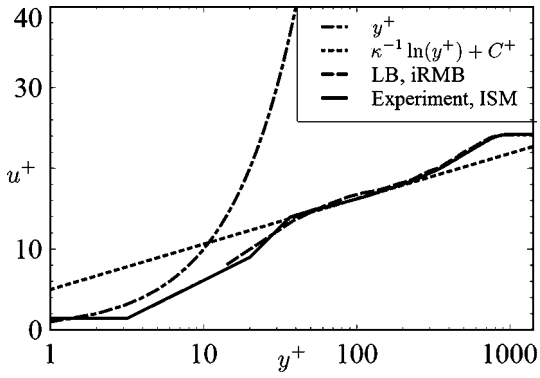

Fig. 11 Time-averaged streamwise velocity profile at 95 % of plate's chord in inner coordinates (designated with +)

with Smagorinsky LES is used. A near-wall damping was introduced at the points closest to the upper surface of the plate.

The simulated time-averaged (mean) velocity is compared with the experimental data of ISM as shown in Fig. 11. The velocity is non-dimensionalized with the wall friction velocity u_τ and the distance y to the wall is measured in wall units $y^+ = yu_\tau/\nu$ involving the kinematic viscosity ν. The first grid node is located 0.13 mm from the plate's surface.

At this first node the velocity is underestimated by 7 %. An underestimation of the near-wall velocity is to be expected for coarse grid resolution in a turbulent boundary layer. The error then quickly diminishes and the velocities match the experiment within measurement uncertainty for a non-dimensional distance of about 150 or more above the plate's surface. A further source of errors are the PIV measurement devices that are fixed on a horizontal beam a few centimeters above and behind the plate and were not modeled. The data also show a fair agreement with the displayed classical logarithmic law in which the values $\kappa = 0.41$ and $C^+ = 5$ were used.

Figure 12 depicts the distribution of some turbulence statistics, namely the RMS values of the streamwise (x) and vertical (y) velocity components as well as the x–y-Reynolds stress, all again in inner units. The offset for the streamwise component (seen at large values of y^+) appears to be due to transient pressure fluctuations. We observed that it is larger for smaller averaging times and expect it to vanish for very large averaging times or improved boundary conditions.

Overall, the agreement with the experimental data is quite encouraging, especially in view of this first application of the LBM to this problem. Errors in the viscous sublayer and the buffer zone are expected to diminish for computations with increased resolutions which are planned in the near future.

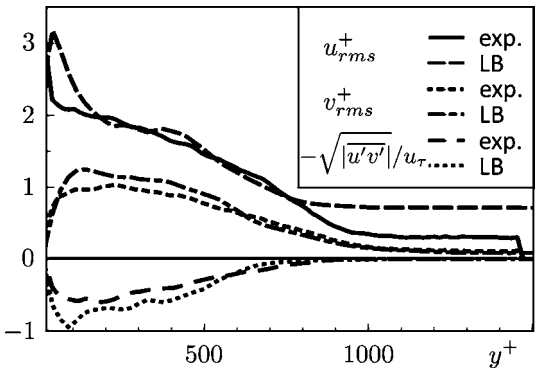

Fig. 12 RMS values of the streamwise (u) and wall-normal (v) velocity components referenced to the wall shear velocity as well as dimensionless cross correlation velocity (uv)

2.1.4 Microstructural characterisation of porous materials

In the SFB 880 a broad range of porous materials, such as superalloy membranes [15, 16], sintered fibre felts, sintered bronze powder, porous aluminium, metallic foams and perforated plates is investigated which covers a pore size range from 500 to 1 mm, a porosity range from 15 to 95 % as well as the cases of statistical and periodical porosity. For the microstructural characterization two-dimensional light and electron microscopy as well as three-dimensional computer tomography (CT) are used. Due to the limited resolution of the CT-scanner only materials with pores and ligaments that are several microns in size, can be three-dimensionally characterized. For materials with a finer structure, two-dimensional light or electron microscopy, that has a much higher resolution, has to be used. The three-dimensional scanning has the advantage to look at more than one plane. Because of that it is possible to take changes in the cross-sectional area of pores and ligaments into account and determine the porosity more precisely. Additionally it is possible to distinguish between open and closed pores. Finally, a three-dimensional image gives a better impression of the material.

For two-dimensional microscopy the samples are embedded into a polymer, grinded and polished. The two-dimensional microscope images are binarized to generate black and white images and smoothed to reduce noise. Afterwards a lattice of lines with a defined distance is superimposed to the images. The lattice is then rotated 180° in steps of 1° and the length of the black and white segments, representing the pores and ligaments respectively, is measured. The porosity is equivalent to the percentage of white pixels in the binarized images. This method is used for the superalloy membranes whose fine structure requires a resolution that can only be reached using electron microscopy. Additionally light microscopy is used to double check the CT results.

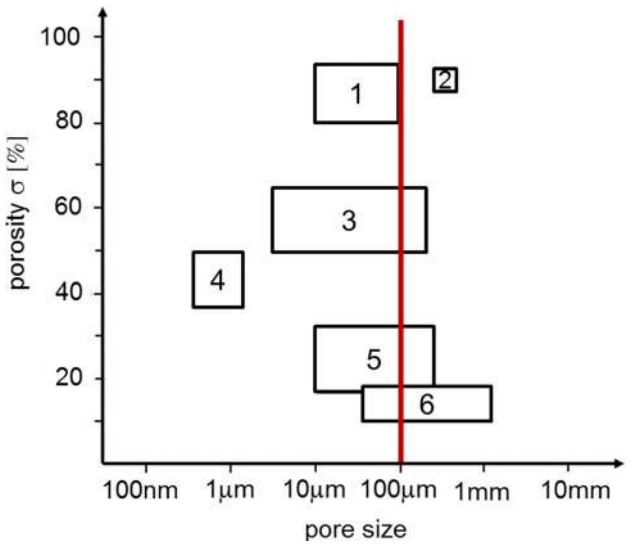

Fig. 13 Porosity and pore size of porous materials. (*1*) sintered fibre felts, (*2*) metallic foam, (*3*) porous aluminium (pore size given by manufacturer), (*4*) superalloy membranes, (*5*) sintered bronze powder [pore size given by manufacturer and determined using the single-pass test (ASTM F795)], (*6*) perforated plates

In the CT scanner two dimensional X-ray images of the samples are taken under different angles while the sample is rotated 360°. In the subsequent reconstruction a three-dimensional image is calculated using the X-ray image stack. For a high resolution the sample needs to be placed close to the X-ray tube. Therefore the optimal samples are small and roughly rotationally symmetric. To prepare the samples the porous materials are cut into square sticks that are about 2 mm thick and kept short to avoid eccentric rotation. The sintered fibre felts and the metallic foam are previously embedded into a polymer to stiffen the material. Thus a voxel size of V = 1 µm is realized. To determine the material parameters a material surface has to be defined by assigning grey values to air, and polymer respectively, or material. Afterwards the microstructure can be measured by fitting cylinders, spheres and circles to the surface or running a defect detection to determine the porosity.

An overview over the material parameters pore size and open porosity of the characterized materials can be seen in Fig. 13. For comparison the vertical line indicates the characteristic width of the trailing edge micro slits investigated in Sect. 2.1.1.

As the porous materials differ in their structure, different parameters are required for the characterization. Figure 14 shows CT images of sintered fibre felts SFF100, 120, 150 and the metal foam350 (properties see Table 1). Unlike for the other materials it is impossible to define a geometric pore size for sintered fibre felts due to their irregular structure. Therefore the fibre radius and porosity are used

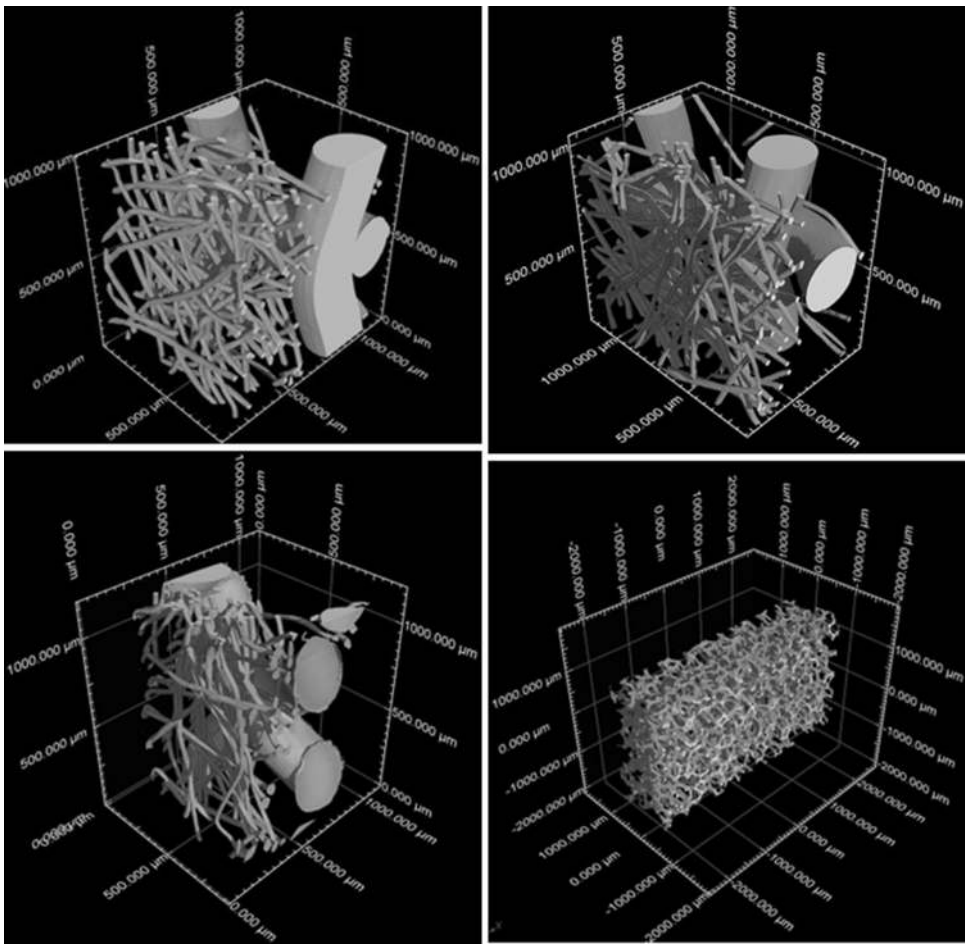

Fig. 14 CT image of sintered fibre felt SFF100 (*top left*), SFF120 (*top right*), SFF150 (*bottom left*) and metal foam M350 (*bottom right*)

to characterize the material. The fibre radius of the sintered fibre felts range from 2 to 12 μm. The pore sizes of the sintered fibre felts used in Fig. 13 are the effective pore diameters given by the manufacturer and established using the "Bubble-Point" principle according to ASTM E 1294 [17].

2.1.5 Aeroacoustic testing of porous material

In order to investigate the ability of the various porous materials to reduce aerodynamic sound generation a 2D model of the wing airfoil of the SFB 880 reference aircraft was equipped with respective trailing edge inserts (see Fig. 15), [32]. The farfield sound radiation was measured with an elliptic mirror focussed on the edge region with and without insert. The spectra depicted in Fig. 15, measured at a flow speed of 50 m/s and at zero angle of attack, indicate that the trailing edge noise reduction success depends on the material. Here, two sintered fibre felts are studied which reveals that the noise reduction in reference to the solid trailing edge increases with decreasing flow resistance of the felt. Moreover, at high frequencies a noise increase is observed due to the roughness induced turbulence increase.

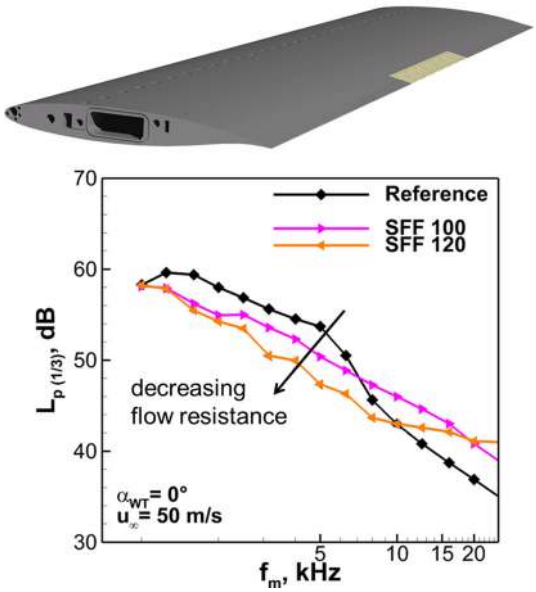

Fig. 15 Acoustic wind tunnel test of sintered fibre felts as inserts into trailing edge of an airfoil (*top*), measured third octave band farfield sound pressure levels

3 Reduction of sound radiation by configuration design

A subsonic propeller unavoidably generates aerodynamic sound according to the aerodynamic loading on its blades and the displacement of air by each blade. The helical blade tip Mach number of the propeller typically results from the performance driven aerodesign. On the other hand it controls the sound radiation of the propeller in undisturbed flow and thus the acoustic source is practically fixed. Given the very low noise requirement on the SFB 880 aircraft concept the sound of its propellers is to be reduced. This task then amounts to using the adjacent aircraft structure as a sound shield to the ground. While a shielding surface is most effective when placed very near the propeller, the aerodynamic installation effects may then generate new acoustic sources due to additional unsteady blade loads, which requires thorough aerodynamic-acoustic analysis. Finally, especially when an aircraft structure is used as a sound shield it will be excited to stronger vibrations, which in turn leads to increased cabin noise. Therefore the vibroacoustic excitation of cabin noise needs to be simulated for solid and porous materials requiring new computation models.

3.1 Integrated propeller for noise shielding

For maximum take-off performance and efficiency at cruise, a turboprop engine was selected to deliver the required thrust. The key parameters of the reference aircraft are given in Table 3. As noise is an issue for open rotors in general, unconventional propeller installation concepts shall either directly or indirectly lead to an acoustically beneficial configuration. The direct way is to mount the propeller over the wing in order to shield the noise which can be perceived at the ground. On the other hand the aerodynamic performance can be optimized for a given engine power to increase the climb angle and thus reducing the noise footprint.

The present section deals with the aerodynamic and aero-acoustic propeller installation effects at the take-off configuration with deployed flaps and presents new ideas of integration [18, 19]. A simplified geometry, consisting of a wing segment and a propeller–nacelle combination, is analysed by means of CFD and compared to the clean wing. Besides the tractor, a channel wing configuration with embedded propeller is considered. The aerodynamic assessment of the overall configuration focuses on the climb angle $\sin\theta = T_{\text{total}}/MTOW - 1/(\text{L/D})$ as an important figure of merit (L/D = lift/drag ratio, MTOW = max. take-off weight). It determines the noise footprint as well as the engine sizing (take-off with one-engine-inoperative).

Table 3 Specifications of the STOL aircraft

Payload	12,000 kg (100 PAX + freight)
Range	2,000 km
Take-off distance	<800 m
$C_{L,\,max}$ (Landing)	3.4
Thrust/Weight T/W (Take-off)	0.49

The profile of the rectangular wing segment is based on the DLR F15 airfoil, with a $0.25c$ long plain Coanda flap at 45° setting [20]. Due to the small wingspan of $b = 5c$, symmetry conditions are applied to the wing tips. The propeller (diameter $D_P = 5\text{ m} = 1.32c$) was simulated by using an actuator disk and a generic nacelle. The baseline channel wing has a moderate embedding depth of $\Delta z_P/D_P = 1/6$ while the propeller is located above midchord ($x_P/c = 0.4$). Four additional positions $x_P/c = \{0.1; 0.25; 0.55; 0.7\}$ were considered for the aerodynamic study. Two of them (0.25 and 0.7) were also used in the aeroacoustic simulations. The operating point is located between the take-off and climb segment with a Mach number of $\text{Ma}_\infty = 0.172$ and a profile lift coefficient of $c_l = 0.31$. The corresponding angle of attack ($\alpha = 0°$) was used for all simulations.

The steady CFD simulations were conducted by using the *DLR TAU code* for solving the RANS equations on the unstructured *Centaur* grids. Turbulence was modeled by the Spalart–Allmaras one-equation formulation. The active actuator disk model uses blade element theory to calculate the steady forces applied to the fluid [21]. This means that the actual inflow is taken into account which is particularly important for installed propellers.

The acoustic interaction of the installed propeller and wing can be considered as a scattering problem which can be solved by the Helmholtz equation (Kirchhoff integrals).

Due to its (at best) $O(N^2)$ scaling (N—number of boundary elements), classical BEM is applicable only for low frequencies. Therefore, accelerated versions have been developed of which the Fast Multipole Method (FMM) is the most efficient one [22, 23]. FMM is an iterative method which reduces the complexity of a matrix–vector product to $O(N \log N)$. The BEM requires the incident pressure field of the propeller on the surface of the body which can be calculated by a model proposed by Glegg [24]. There, the loading noise of the propeller is represented by rings of dipoles on the propeller disk, ref. Fig. 16. The dipole strength is obtained from the blade forces obtained by the TAU calculations.

Aerodynamic results. It is shown in [18] that an over-the-wing propeller suffers from inhomogeneous inflow conditions at increased velocity level. At constant shaft power, the channel wing propeller loses 20 % of thrust and efficiency. In addition, the thrust distribution is heavily shifted upwards, away from the wing, see Fig. 17.

Considering the midspan pressure distribution of the tractor configuration (Fig. 18), the increased suction peak

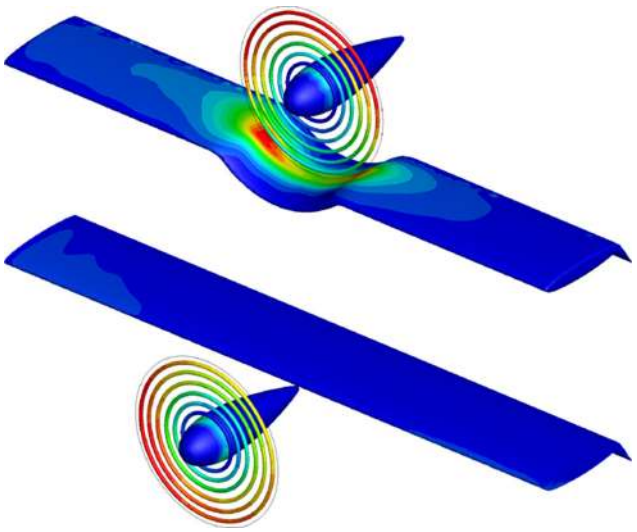

Fig. 16 Acoustic model, showing local propeller non-uniform thrust forces and sound pressure on channel wing (*top*) and tractor wing (*bottom*)

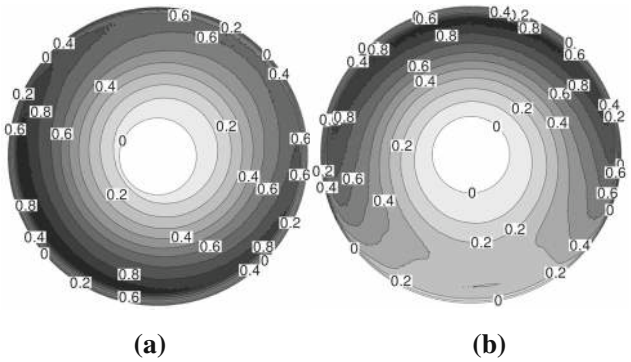

Fig. 17 Propeller disk distributions of relative thrust t/t_{max} at constant shaft power coefficient. **a** Tractor $\eta_p = 0.61$, **b** channel wing $\eta_p = 0.49$

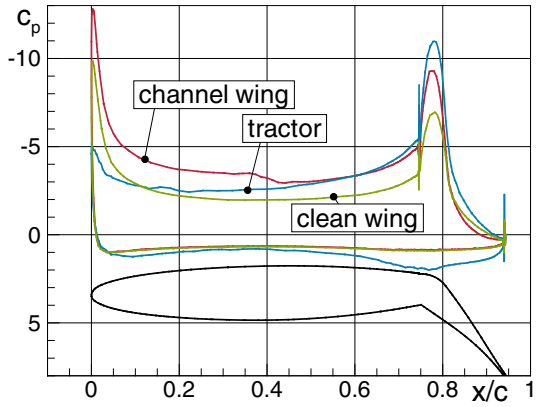

Fig. 18 Pressure distribution at midspan

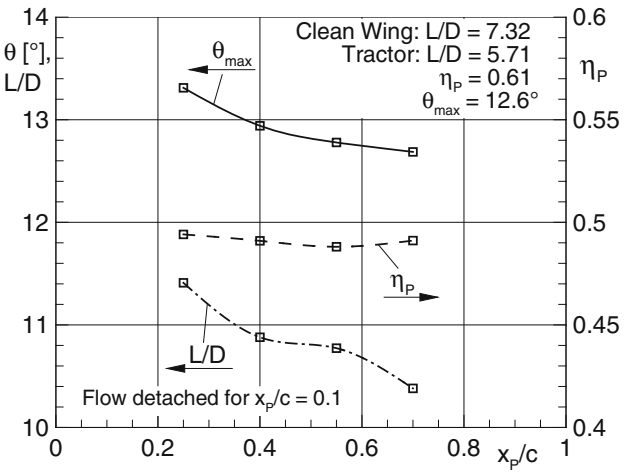

Fig. 19 Aerodynamic performance parameters

on the Coanda flap (compared to the clean wing) gives evidence of a propeller slipstram deflection mechanism. Together with a high pressure area at the hinge, most of the additional lift is generated on rear surfaces which induce pressure drag. The channel wing behaves completely different as the propeller installation leads to additional suction forces in the front region of the wing. This effect induces a thrust force which lowers the overall drag of the configuration.

Transferring the increments in thrust, lift and drag (due to propeller installation) to the reference aircraft, one can calculate the lift-to-drag ratio, propeller efficiency and climb angle of the aircraft. This was done for five different axial positions of the propeller. The results of four of these are shown in Fig. 19. The length of the front suction peak increases with x_P/c while its magnitude at the leading edge decreases. Considering the local surface orientation, this means a relative reduction in forward-pointing suction forces for the rearmost propeller position which contributes to drag and thus lowers L/D. As the propeller efficiency is relatively constant, the climb angle is mainly influenced by the gradient of the lift-to-drag ratio. At least aerodynamically, a favorable design is found for a propeller installation around 25 % wing chord as the 10 % position leads to flow separation (not shown).

Aeroacoustic results. Figure 20 shows the sound pressure level (SPL) in a plane 120 m below the configurations. The wing is located in the origin and the propeller axis points to the left. The propeller radiates predominantly to the right side of the wing. For the channel wing cases, the shielding effect decreases with increasing chord position of the propeller. The maximum SPL value in the $x_P/c = 0.7$ position is about 96 dB and thus a little bit higher than that

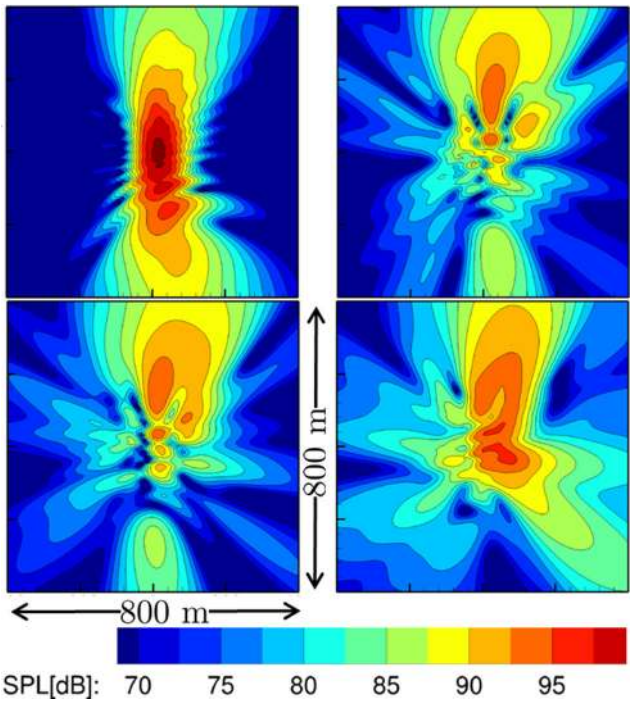

Fig. 20 Noise contours 120 m below the aircraft, *top left* tractor, *top right* channel wing 25 %, *bottom left* channel wing 40 %, *bottom right* channel wing 70 %

of the forward positions (about 95 dB). In the tractor position, the propeller noise is unshielded, and the SPL reaches up to 101 dB.

This means that the aerodynamic and aeroacoustic optimum regarding the axial position of the propeller appear to be the same.

3.2 Vibroacoustic behavior of porous material

The aim of the work of IK is to model the vibroacoustic behavior of porous materials. Perforated plates and sintered fibre felts are studied. To model the Sintered Fibre Felts (SFF), first some material parameters are determined. The tortuosity and the viscous und thermal characteristic length are obtained from absorption coefficient measurements using a curve fitting optimization method based on the Least-Squares Levenberg–Marquard [29, 30] method. To simulate the absorption coefficient of the SFF the Biot's model is used [25]. To predict the behavior of the microperforated plates (MPP), an approach proposed by Atalla and Sgard is implemented. This model is based the Johnson–Allard method for rigid frame porous media [26] and a curve fitting method is not required. The measurements are obtained in an impedance tube and as a computational method the transfer matrix method is used in both cases [25, 31].

Sintered fibre felts. Biot's model offers a complete description of the wave propagation through porous materials, considering the solid phase, the fluid phase and the interaction between them. Here, Biot's model for poroelastic materials in the corresponding (u, p)—formulation is used. The variables of the formulation are the deflections u and the sound pressure p.

$$\hat{\sigma}^s_{ij,j} + \tilde{\rho}\omega^2 u^s_i + \tilde{\gamma} p_{,i} = 0 \tag{1}$$

$$\tilde{\gamma} = \phi\left(\frac{\tilde{\rho}_{12}}{\tilde{\rho}_{22}} - \frac{\tilde{Q}}{\tilde{R}}\right) \quad \text{and} \quad \tilde{\rho} = \tilde{\rho}_{11} - \frac{\tilde{\rho}^2_{12}}{\tilde{\rho}_{22}} \tag{2}$$

The equation of motion for the fluid phase is given by

$$p_{,ii} + \frac{\tilde{\rho}_{22}}{\tilde{R}}\omega^2 p - \frac{\tilde{\rho}_{22}}{\phi^2}\tilde{\gamma}\omega^2 u^s_{i,i} = 0. \tag{3}$$

$\hat{\sigma}^s_{ij}$ denotes the stress tensor of the solid phase and ϕ the porosity. The indices s and f correspond to the solid and fluid phase, $\tilde{R}$ the bulk modulus of the air occupying a fraction ϕ. The tilde symbol indicates frequency dependency. $\tilde{Q}$ is a coupling coefficient between the dilatation and stress of the two phases, $\tilde{\rho}$ is the effective density. The densities $\tilde{\rho}_{11}$ and $\tilde{\rho}_{22}$ are mass coefficients which take into account the fact that the relative flow though the pores is not uniform. They are related to the mass density of the material of the solid phase and to the mass density of the fluid. $\tilde{\rho}_{12}$ represents the interaction between the inertia forces of the solid and the fluid phases [25]. Detailed description of Biot's model can be found in [27]. In Table 4, the material parameters of SFF100 and SFF150 are presented.

In this table the values denoted with (*) and (**) were determined from computer tomographic images and from light microscope images (Sect. 2.1.4), respectively. The values for the flow resistivity σ were measured using the alternating airflow method (Method B DIN EN 29053 [28]) in Physikalisch Technische Bundesanstalt—PTB in Braunschweig, Germany and the rest of the values were obtained using the prediction method described above. In Fig. 21, the acoustic behavior of SFF100 and SFF150 is presented. The results of the simulation carried out with the transfer matrix method are compared with the absorption coefficient measurements. Solid and dashed lines represent the sound absorption simulation of SFF100 and 150, respectively. Measurements are presented with small stars.

Perforated plates. The effect and behavior of the perforated plates are mainly dependent on the porosity, flow resistivity, perforation thickness and mounting condition. To model perforated plates, an approach based on the Johnson-Allard for rigid frame porous media by Atalla and Sgard is used. Biots parameters for cylindrical pores and an equivalent tortuosity are assumed [26]. The used mounting configuration is shown in Fig. 22.

The configuration consists of a perforated plate with thickness h, separated from a hard wall by an air cavity. For

Table 4 Material parameters

	SFF100	SFF150	MPP3	MPP4
h (mm)	0.43*	0.74*	0.64**	0.55**
σ (Pa × s/m^2)	56,956	18,913	234,844	767,291
ϕ (−)	0.92*	0.937*	0.18*	0.140*
r (mm)	0.0125*	0.0125*	0.05**	0.03**
α_∞ (−)	1.1778	1.1163	1.069	1.053
Λ (mm)	3.8271e−5	6.9529e−5	5.90e−5	3.7e−5
Λ' (mm)	1.6123e−4	1.6211e−4	5.90e−5	3.70e−5

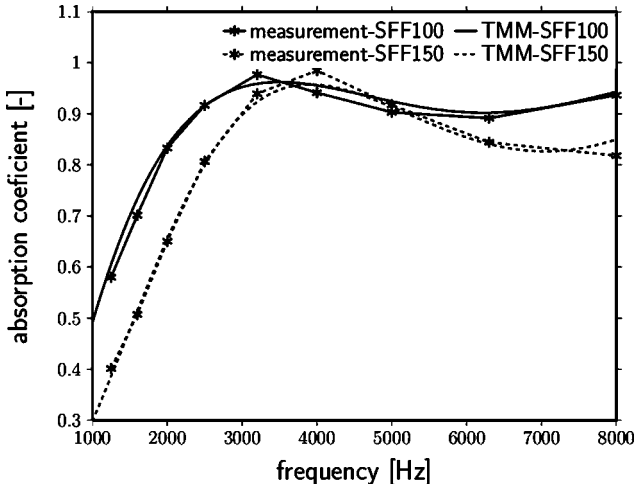

Fig. 21 Absorption coefficient. Sintered fibre felts

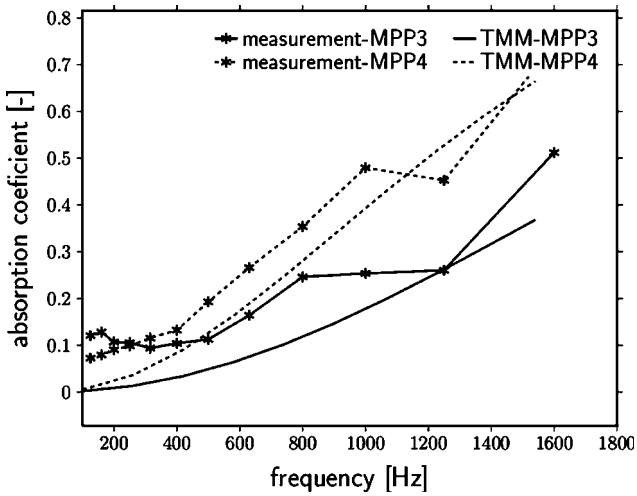

Fig. 23 Absorption coefficient. Perforated plate

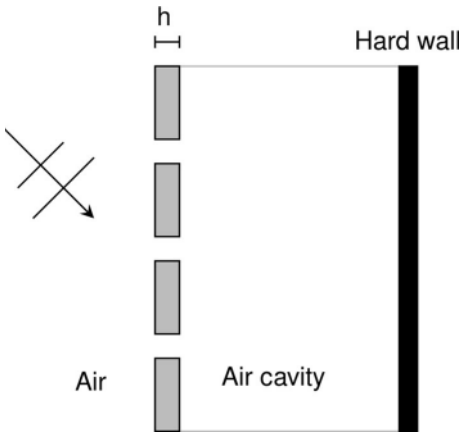

Fig. 22 Perforated plate mounting configuration

straight cylindrical pores the flow resistivity $\sigma = 8\mu/\phi r^2$, is related to the perforation radius of the pore r and the porosity ϕ, where μ is the dynamic viscosity of air. The viscous and the thermal characteristics lengths, Λ and Λ', respectively, are equal to the hydraulic radius of the pore [25]. In order to take into account the distortions of the flow induced by the perforations, the tortuosity of the perforated plates must be corrected depending on the media in which the perforated system radiates [26].

$$\alpha_\infty = 1 + 2\varepsilon_e/h \tag{4}$$

$$\varepsilon_e = 0.48\sqrt{\pi r^2}(1 - 1.44\sqrt{\phi}) \tag{5}$$

The equivalent tortuosity is presented in Eq. (4). The correction term ε_e, is a function of the correction length associated the radiation of a circular piston in free air together with the tortuosity of the medium in which the perforated plate radiates [26] and it is presented in Eq. (5).

To validate the implemented model, the sound absorption measurements of two perforated plate samples are used. The mounting configuration is shown in Fig. 22 and the material parameters are listed in Table 4. Figure 23 depicts the sound absorption simulation of MPP3 and 4 as solid and dashed lines respectively. Measurements are presented with small stars. The sound absorption simulation results are satisfactory, although with a clear tendency of under prediction for most of the frequency range. Especially the differences in the absorption coefficient of the two materials are captured well by the theoretical model.

4 Conclusions

CAA simulations of slotted trailing edges of airfoils (representing porous materials) show that the cancellation of the anti-phase pressure signals from suction and pressure in the nearfield of the source is responsible for the noise reduction. A volume-averaged RANS model for compressible turbulent flow past porous media has successfully been developed to provide flow and turbulence input to CAA computations. Flow through spatially resolved porous material could be simulated successfully on the basis of LBM simulations. As a first step prior to solving the combined problem the turbulent plate boundary layer was successfully simulated separately with the same method using an LES approach. Various porous materials for aero acoustic use were micro-structurally characterized based on computer tomography and electron microscopy. First aeroacoustic test show that trailing edge noise reduction increases with decreasing flow resistance of the applied porous material. The combined aero-acoustic investigation of a highly integrated propeller (over- and channel wing) show aerodynamic and acoustic benefits for low speed but reveal strong drawbacks for the targeted cruise flight of the SFB aircraft concept. Sintered fibre felt and perforated plate type porous materials were vibroacoustically modeled for further assessment of cabin noise excitation of SFB 880 type aircraft.

Acknowledgments This work was funded by the Deutsche Forschungsge-meinschaft DFG (German Research Funding Organisation) in the framework of the collaborative research centre SFB 880. Computational resources were provided by the North-German Supercomputing Alliance HLRN.

References

1. Delfs, J.: Aerodynamisches Bauteil mit einer geschlitzten Hinter- oder Seitenkante (aerodynamic device with slotted trailing- or side edge, German patent DE 10 2006 049 616 A1, submitted 20.10.2006, German Patent Authority (2010)
2. Herr, M.: Design criteria for low-noise trailing edges. In: 13th AIAA/CEAS Aeroacoustics Conference, AIAA Paper 2007-3470
3. Faßmann, B., Delfs, J., Ewert, R., Dierke, J.: Reduction of emitted sound by application of porous trailing edges. In: Radespiel, R., Semaan, R.: SFB 880—Fundamentals of High-Lift for Future Commercial Aircraft, Biennial Report. TU Braunschweig, Campus Research Airport, (2013)
4. Ewert, R., Dierke, J., Siebert, J., Neifeld, A., Appel, C., Siefert, M., Kornow, O.: CAA broadband noise prediction for aeroacoustic design. J Sound Vib **330**, 4139–4160 (2011)
5. Whitaker, S.: The Method of Averaging. Kluwer Academic, Dordrecht (1999)
6. Wilcox, D.C.: Turbulence Modeling for CFD, 3rd edn. DCW Industries, Canada (2006)
7. Cécora, R.-D., Eisfeld, B., Probst, A., Crippa, S., Radespiel, R.: Differential reynolds stress modeling for aeronautics, In: 50th AIAA Aerospace Sciences Meeting, (2012)
8. Lemos, M.J.S., Silva, R.A.: Turbulent flow over a layer of a highly permeable medium simulated with a diffusion-jump model for the interface. Int. J. Heat Mass Transf. **49**, 546–556 (2006)
9. Schwamborn, D., Gerhold, T., Heinrich, R.: The DLR TAU-Code: recent applications in research and industry, IN: European Conference on Computational Fluid Dynamics, ECCOMAS CFD 06, (2006)
10. Breugem, W.-P.: The influence of wall permeability on laminar and turbulent flows, PHD thesis, Technische Universiteit Delft, Delft (2005)
11. Mößner, M., Radespiel, R.: Numerical Simulations of turbulent flow over porous media, AIAA2013-2963, 21st AIAA Computational Fluid
12. Ahrenholz, B., Tölke, J., Lehmann, P., Peters, A., Kaestner, A., Krafczyk, M., Durner, W.: Prediction of capillary hysteresis in porous material using lattice Boltzmann methods and comparison to experimental data and a morphological pore network model. Adv. Water Resour. **31**, 1151–1173 (2008)
13. Freudiger, S.: Entwicklung eines parallelen, adaptiven, komponentenbasierten Strömungskerns für hierarchische Gitter auf Basis des Lattice-Boltzmann–Verfahrens. PHD thesis, TU Braunschweig, Germany, (2009)
14. Ducros, F., Comte, P., Lesieur, M.: Large-eddy simulation of transition to turbulence in a boundary layer developing spatially over a flat plate. J. Fluid Mech. **326**, 1–36 (1996)
15. Rösler, J., Näth, O., Jäger, S., Schmitz, F., Mukherji, D.: Fabrication of nanoporous Ni-based superalloy membranes. Acta Mater. **53**, 1397–1406 (2004)
16. Hinze, B., Rösler, J., Schmitz, F.: Production of nanoporous superalloy membranes by load-free coarsening of γ'-precipitates. Acta Mater. **59**, 3049–3060 (2011)
17. GKN Sinter Metals, [Online]. Available: http://gkn-filters.de/downloads/pdf/download.php?filename=metal-fibre-felt-fil.pdf. [Accessed 1 October 2010]
18. Müller, L., Kozulovic, D., Hepperle, M., Radespiel, R.: Installation effects of a propeller over a wing with internally blown flaps, In: Proceedings of the 30th AIAA Applied Aerodynamics Conference, Paper AIAA 2012-3335, New Orleans (2012)
19. Müller, L., Kozulovic, D., Hepperle, M., Radespiel, R.: The Influence of the propeller position on the aerodynamics of a channel wing, In: Proceedings of Deutscher Luft- und Raumfahrtkongress 2012, Berlin, Germany, (2012)
20. Jensch, C., Pfingsten, K.-C., Radespiel, R., Schuermann, M., Haupt, M., Bauss, S.: Design aspects of a gapless high-lift system with active blowing, In: Proceedings of Deutscher Luft- und Raumfahrtkongress 2009, Aachen, Germany, (2009)
21. Raichle, A., Melber-Wilkening, S., Himisch, J.: A new actuator disk model for the tau code and application to a sailplane with a folding engine, In: Proceedings of the 15th STAB/DGLR Symposium, Darmstadt, Germany, (2006)
22. Coifman, G., Rokhlin, V., Wandzura, S.: The fast multipole method for the wave equation: a pedestrian prescription. IEEE Antennas Propag. Mag. **35**(3), 7–12 (1993)
23. Sylvand, G.: Performance of a parallel implementation of the FMM for electromagnetics applications. Int. J. Num. Meth. Fluids **43**(8), 865–879 (2003)
24. Glegg, S.A.L.: Effect of centerbody scattering on propeller noise. AIAA J. **29**(4), 572–576 (1991)
25. Allard, J.F., Atalla, N.: Propagation of sound in porous media. John Wiley & Sons Ltd, New York (2009)
26. Atalla, N., Sgard, F.: Modelling of perforated plates and screens using rigid frame porous models. J. Sound Vib. **303**, 195–208 (2007)
27. Atala, N., Panneton, R., Debergue, P.: A mixed displacement–pressure formulation for poroelastic materials. J. Acoust. Soc. Am. **104**, 1444–1452 (1998)

28. DIN 29053: Acoustics; material for acoustical applications; Determination of airflow resistance (ISO 9053:1991). German version EN 29053:1993, (1993)
29. Levenberg, K.: A method for the solution of certain problems in least squares. Q. Appl. Math. **2**, 164–168 (1944)
30. Marquardt, D.: An algorithm for least-squares estimation of nonlinear parameters. SIAM J. Appl. Math. **11**, 431–441 (1963)
31. Rurkowska, K., Langer, S.: Prediction of acoustic behaviour of microperforated plates in high-lift configuration. In: Proceedings of DAGA 2013, Meran-Italy (2013)
32. Herr, M., Rossignol, K.-St., Delfs, J, Mößner, M., Lippitz, N.: Specification of porous materials for low noise trailing edge applications. In: AIAA Paper 2014–3041, 20th AIAA/CEAS Aeroacoustics Conference, Atlanta, GA (2014)